BUTTERWORTH HEINEMANN

Experimental and computational study of turbulent heat transfer characteristics in serrated channel flow

S. Obi
Department of Mechanical Engineering, Keio University, Yokohama, Japan

K. P. Kobayashi, A. M. Bethancourt, H. Yoshida, T. Asano, and R. Echigo
Department of Mechanical Engineering and Science, Tokyo Institute of Technology, Tokyo, Japan

A two-dimensional (2-D) channel with a serrated wall is proposed as a device for heat transfer augmentation. Measurements of the flow velocity in the whole field as well as of the heat transfer coefficient along the wall are undertaken for two different channel heights. The same flow fields are calculated using a second-moment closure and the standard k-ε model. The flow field containing successive separation and reattachment partly resembles the conventional backward-facing step flow, although the extremely high turbulence level found in the present configuration indicates a promising performance of the serrated channel as a heat transfer promoter.

Keywords: turbulent flows; separation and impingement; heat transfer augmentation; laser Doppler anenometry measurements; application of turbulence models

Introduction

It is well known that heat transfer is considerably augmented around the flow reattachment point; e.g., behind a backward-facing step. This heat transfer enhancement is basically ascribed to stagnation-point flow with intense turbulence generated and convected along the separated shear layer. It is, therefore, desirable that the turbulence intensity reaches its maximum near the wall, when efficient use of the turbulent fluid motion is considered for the promotion of convective heat transfer. Measurements of backward-facing step flows in the past (e.g., Etheridge and Kemp 1978; Kim et al. 1980) indicate, however, that the maximum of turbulent kinetic energy; i.e., the fluid portion associated with the most intense turbulent motion, is convected almost parallel to the main flow and does not impinge onto the wall.

Serrated-wall channel flow, see Figure 1a, is considered to be one of the basic configurations that effectively uses the above-mentioned turbulent fluid motion. Because of the contraction of channel width downstream of the separation point, the turbulent motion developing along the separated shear layer has more chance to come into contact with the surface of both sides of the channel than in a parallel channel. It is, therefore, expected that more heat transfer augmentation is achieved as compared with the backward-facing step flow. An example of practical application to a counterflow heat exchanger is shown in Figure 1b.

Serrated-wall channel flow is also an important test case for turbulent flow calculation procedures. Its complex features include flow separation, reattachment, and wall-attached flow under the influence of varying streamwise pressure gradient, and the assessment of turbulence models can be conducted in terms of precise representation of these characteristics. From a numerical point of view, it is, again, an attractive problem, because the inclined wall of the serration hinders the use of conventional orthogonal grids that requires a more advanced numerical technique. Another advantage of this flow field as a test case for turbulent flow calculation is that the inlet boundary condition can be specified precisely. Because attention is paid to fully developed flow field, the ambiguity of the results due to the inlet boundary condition, which is often the case, e.g., for the backward-facing step flow, can be avoided, and pure assessment of the turbulence models is possible.

The objective of the present study is to clarify the flow and heat transfer characteristics of the serrated channel flow both experimentally and numerically. The calculations using turbulence models are performed using a second-moment closure and the k-ε model, and the ability to represent the development of a separated shear layer is discussed in connection with the performance of the serrated channel as a heat transfer promoter.

Experiments

Flow configuration

As shown in Figure 2a, the two-dimensional (2-D) air duct serving as the test section was 300 mm in width and 2000 mm in total length. The serrated wall was placed on the bottom side of the duct. The serration consisted of 11 steps 20 mm high and 160 mm long, giving the resultant slant angle of about 7°. The step height H_S and length L_S were determined in light of the fact that the reattachment point is located about seven step heights down-

Address reprint requests to Prof. S. Obi, Department of Mechanical Engineering, Keio University, 3-14-1 Hiyoshi Kohoku-ku, Yokohama 223, Japan.

Received 27 January 1995; accepted 12 May 1995

Int. J. Heat and Fluid Flow 16: 398–404, 1995

655 Avenue of the Americas, New York, NY 10010

0142-727X/95/$10.00
SSDI 0142-727X(95)00048-U

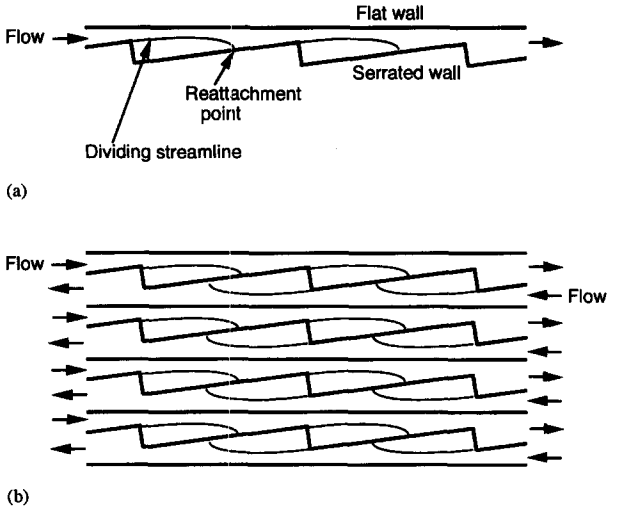

Figure 1 Schematics of the serrated-wall channel: (a) geometric configuration; (b) example of application to heat exchanger

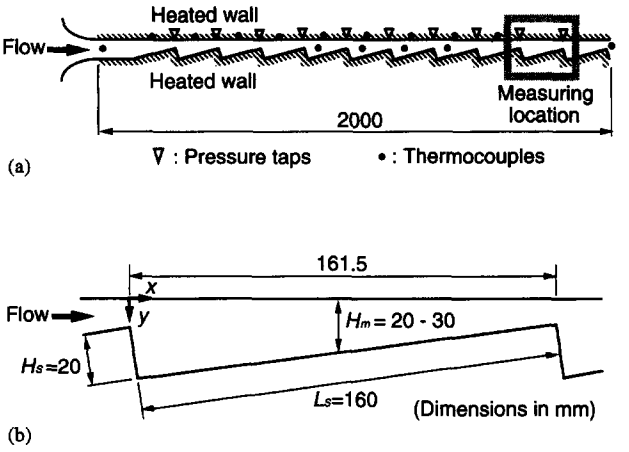

Figure 2 Experimental setup: (a) schematics of the whole channel; (b) definition of the coordinate system

stream of the separation point for the backward-facing step flows (Eaton and Johnston 1981). As shown in Figure 2b, the origin of the Cartesian coordinate was taken at the minimum-height location on the flat wall (the upper side of the duct), with x- and y-axes taken in the streamwise and transverse directions, respectively. The velocity measurements were undertaken for two different mean channel heights $H_m = 20$ mm and 30 mm. The bulk Reynolds number was kept constant at $\mathrm{Re} = U_m H_m/\nu = 1.2 \times 10^4$, with U_m being the bulk mean velocity. The channel with lower height was of primary concern in the present study, because higher turbulence level was expected in this configuration.

Instruments

The flow rate was monitored by an orifice during the measurements and kept constant within the accuracy of 1%. All measurements were made around the 10th step where both the flow and temperature fields were fully developed; their developments were checked by measurements using regularly distributed pressure taps and thermocouples, as shown in Figure 2a. The test section for flow measurements was constructed of transparent acrylic resin. A two-beam, one-component laser Doppler anenometry (LDA) system with a frequency shifter was used to obtain the mean and fluctuating velocity components in the streamwise direction. Micron-sized talc particles were added to provide seeding for the LDA. The surface pressure distribution was measured through the taps of 1 mm diameter using a pressure transducer. The two-dimensionality of the flow field was confirmed over 90% of the channel span.

To conduct the heat transfer experiment, the upper and lower duct walls were replaced by heat transfer measurement plates that consisted of stainless steel foil of 30 μm thickness, which was glued smoothly to a backing. Alternating current was supplied to the foil to provide constant heat flux $q_w = 4000$ W/m^2. For the wall temperature measurement, thermocouples (type T, 0.1 mm diameter) were embedded under the stainless steel foil. On the other hand, the bulk temperature was obtained by interpolating the air temperatures at five locations upstream and downstream of the measuring location. Conduction through the back insulation was estimated to be less than 3% of the total heat transfer from the foil.

Notation

A	heat transfer area of the serrated channel
A_0	heat transfer area of a two-dimensional channel
C_f	skin friction coefficient
C_P	pressure coefficient
F_k	flux of turbulent kinetic energy
F_k^*	normalized value of F_k, $(F_k - F_{k0})/F_{k0}$
F_{k0}	F_k at $x = 0$
f	friction factor, $-(\mathrm{d}P/\mathrm{d}x)H_m/(1/2\rho U_m^2)$
H	channel height
H_m	average channel height
H_S	step height
k	turbulent kinetic energy
L_S	step length
Nu	Nusselt number
Nu_m	Mean Nusselt number of the serrated channel flow
Nu_{m0}	mean Nusselt number of a two-dimensional channel flow
P	static pressure
P_0	reference pressure
q_w	heat flux
Re	Reynolds number $U_m H_m/\nu$
T_b	bulk temperature
T_w	wall temperature
U_m	bulk mean velocity
U	streamwise mean velocity component
$\overline{u^2}$	streamwise normal component of Reynolds stress
x, y	Cartesian coordinates

Greek

γ	weighting factor for convective fluxes
ε	dissipation rate of turbulent kinetic energy
λ	thermal conductivity of fluid
ν	kinematic viscosity of fluid
ρ	fluid density

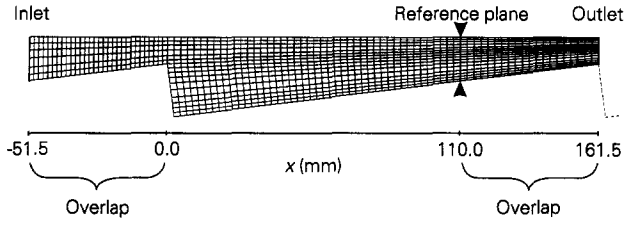

Figure 3 Computation domain and grid arrangement

Computation

Mathematical model

The problem considered here is a steady 2-D flow of incompressible fluid, and Reynolds number is assumed to be sufficiently high so that viscous transport terms may be neglected. The mean flow field is governed by the continuity equation and momentum equations in two directions. Reynolds stresses appearing in the momentum equations are calculated by making use of a basic version of second-moment closures (Gibson and Launder 1978) and the standard k-ε model (Launder and Spalding 1974) in their original form and model constants. For the second-moment closure calculations, the model transport equations are solved for four Reynolds stress components, including three normal and one shear component, and for dissipation rate of turbulent kinetic energy.

Boundary conditions

The computation domain covers about one and one-third period of the serration pitch, as shown in Figure 3. Because of the nature of the present flow, a periodic treatment has been introduced to specify the inlet flow condition; iterative computation procedures are started with arbitrary profiles for each variable. After each iteration, the inlet profiles are replaced by those at the reference plane (see Figure 3) appropriately interpolating the values onto the desired grid points. It should be noted that the mass flux is controlled at every iteration for conservation of the total flow rate. In this manner, the fully developed state can be automatically achieved with the converged solution. At the outlet plane of the integration domain, the streamwise gradient of each variable is kept constant. The solutions in the two overlap regions are thus nearly identical; the comparison of the streamwise mean velocity and turbulence quantities at two corresponding locations in the overlapping regions has confirmed that the inevitable discrepancy due to the difference in grid numbers is less than the estimated solution error described later.

The boundary condition along the solid walls is specified according to the wall function approach (Launder and Spalding 1974) by which the wall shear stress is expressed as a function of the wall-parallel mean velocity component and turbulence kinetic energy at wall-adjacent locations. The mean velocity gradients appearing in the model transport equation of turbulence quantities are evaluated from the same wall law; for the inclined wall, the mean velocity gradient normal to the wall is first calculated according to the conventional wall law and then transformed onto the Cartesian system. The production rates and some of the redistribution terms in the second-moment closure are obtained in this manner. Since it is recognized that the use of wall function may cause ambiguities in the results, the discussion below concentrates mainly on the calculation of the separated turbulent shear layer away from the wall.

Numerical method

A finite-volume method with the collocated variable arrangement employing nonorthogonal grids was used to solve the equation system (Obi et al. 1991; Obi and Perić 1991). The pressure and

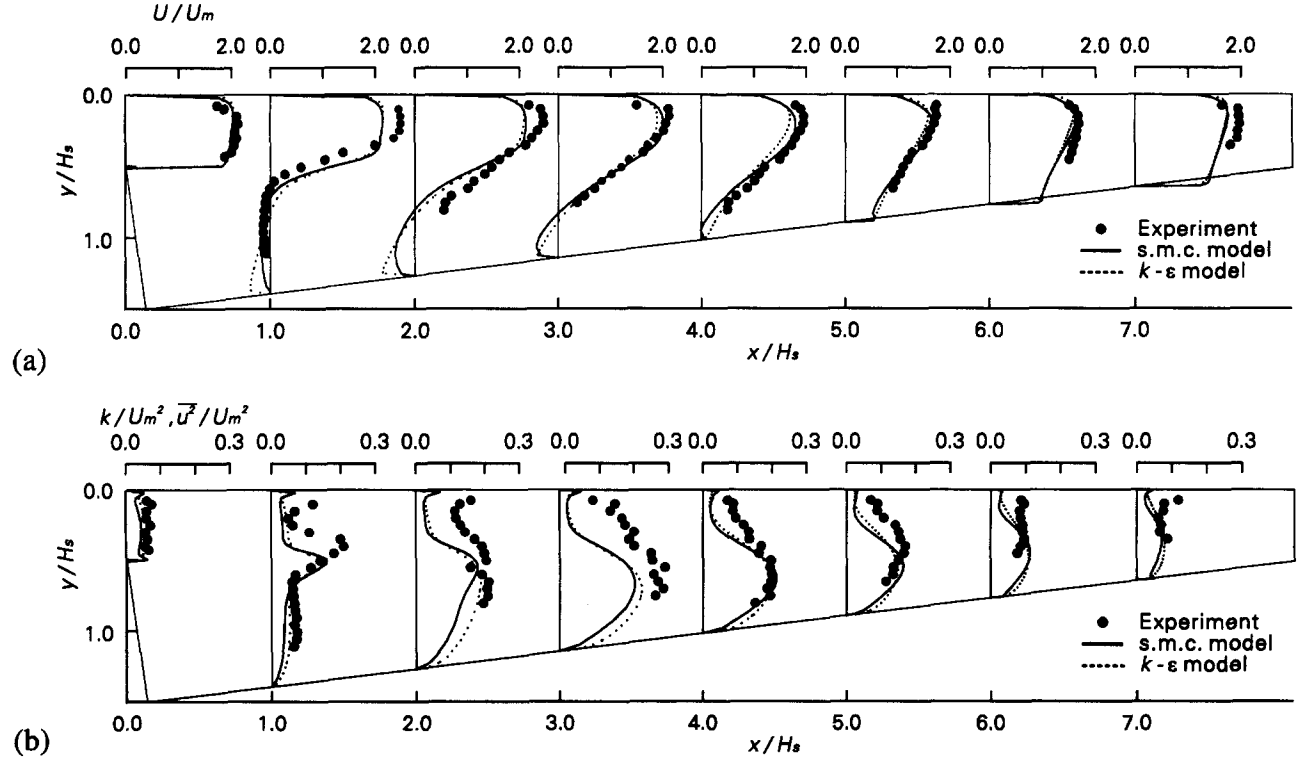

Figure 4 Velocity field for $H_m = 20$ mm: (a) streamwise mean velocity component; (b) normal component of Reynolds stress in streamwise direction

mean velocity fields are coupled by the SIMPLE algorithm of Patankar and Spalding (1972). The convection terms are discretized first by the first-order upwind differencing scheme and then corrected by the second-order central differencing scheme in a deferred-correction manner (Khosla and Rubin 1974). The contribution of the central differencing scheme is controlled by the weighting factor γ that ranges in $0.0 \leqslant \gamma \leqslant 1.0$, where the two limiting values correspond to the pure upwind and pure central differencing schemes, respectively. In general, calculations with high γ values are possible only for low cell Pecret number; i.e., on a grid with satisfactory resolution. During the present calculations, γ is first set equal to zero, then gradually increased. The calculations with $0.5 < \gamma$ yield oscillatory velocity profiles near the step even on the finest grid; hence, the value of γ is restricted to be below 0.5 in the present results.

To estimate the solution errors contained in the results, the computations are performed on three different grids consisting of 47×8, 94×16, and 188×32 control volumes in x- and y-directions, respectively, and the results are compared. Figure 3 illustrates the intermediate-size grid arrangement for the case of the lower channel. From the comparison of the results on a different grid size, it is found that large solution error is concentrated near the separation point, where the mean velocity gradient becomes largest. The maximum error in the mean velocity component and turbulent kinetic energy are estimated to be on the order of $0.1U_m$ and $0.05U_m^2$, respectively. However, in most of the integration domain, they are reduced to $0.01U_m$ and $0.003U_m^2$, respectively.

Results and discussion

Velocity field

Streamwise component of the mean velocity and the turbulent normal stress are presented in Figures 4 and 5 for different channel heights. The measured reattachment length on the bottom wall is approximately $4H_s$ for both cases. This is relatively short compared with that of the backward-facing step flows. In general, the reattachment length is a function of geometric parameters, such as channel expansion ratio, as well as of dynamic parameters; e.g., Reynolds number and oncoming boundary-layer thickness. At sufficiently high Reynolds numbers, the reattachment length reaches a nearly constant value (Armaly et al. 1983), which depends on the channel expansion ratio (Tropea 1983). The reattachment length for the backward-facing step flow with expansion ratio comparable to that in the case of the lower channel reaches as far as eight step heights. This considerable discrepancy in terms of the reattachment length leads us to conclude that the serrated-channel flow is fundamentally different from conventional backward-facing step flows.

The principal cause of the relatively short reattachment length in the present flow problem is considered to be the existence of the inclined wall on the opposite side of the step, a similar feature of which is suggested by the experiment of Driver and Seegmiller (1985). Another probable reason for the short reattachment length is the high turbulence level at the separation point. According to Isomoto and Honami (1989), the reattachment length is substan-

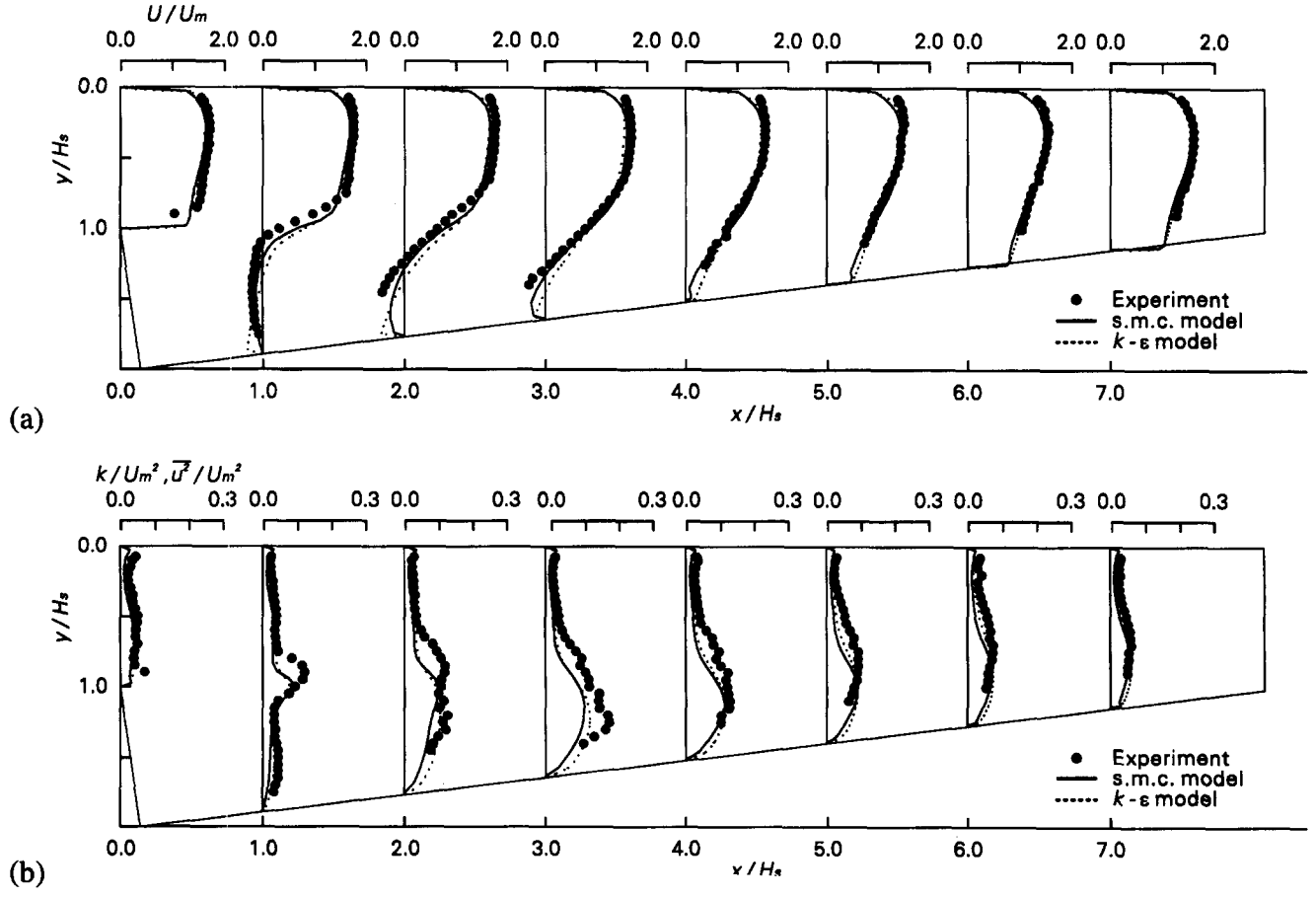

Figure 5 Velocity field for $H_m = 30$ mm: (a) streamwise mean velocity component; (b) normal component of Reynolds stress in streamwise direction

tially reduced when the turbulence level at the separation point is extremely high. In the present flow, as shown by the turbulence intensity profiles for $H_m = 20$ mm, the turbulence level at the separation point becomes very high because of the preceding serration step.

Owing to the reduction of the reattachment length, the region of high turbulence intensity is not located as close to the flat wall as expected, even in the case of the lower channel shown in Figure 4b. The most notable difference due to the channel height is seen along the flat-wall side of the channel in the region $2 \leqslant x/H_s \leqslant 4$; the mean velocity profiles for the lower channel case in Figure 4a show a trend similar to that of wall jets, while their counterparts in Figure 5a yield the core flow region of nearly uniform velocity and relatively low turbulence intensity. The turbulent kinetic energy generated along the separated shear layer with steep velocity gradient thus reaches the flat-wall side only for $H_m = 20$ mm (Figure 4b), while the flat-wall side is unaffected by the high-turbulence field for $H_m = 30$ mm (cf. Figure 5b).

The computational results by both turbulence models are compared in the same figures. It should be noted that the results of the experiment and the second-moment closure are shown for $\overline{u^2}$, while the k-ε model represents turbulent kinetic energy. The overall agreement with the experiment is satisfactory, although there exist some essential shortcomings of turbulence models, which are discussed later. The numerically obtained reattachment lengths are summarized in Table 1 for both channels. Although the second-moment closure provides consistently larger values, the agreement with the experiment is satisfactory for both models.

For the lower channel $H_m = 20$ mm, both turbulence models provide similar results in terms of the mean velocity component, with an exception in the region just behind the step. At $x/H_S = 1.0$, the opposite tendency of the two turbulence models is seen in the recirculation zone; the second-moment closure yields reverse flow increasing with distance from the wall, which is in good agreement with the experiment, while the k-ε model predicts the maximum reverse velocity adjacent to the bottom wall, resulting in mean velocity gradient of the opposite sign. This discrepancy between these turbulence models is common in calculating this type of flow. From a number of experiments on recirculating flow behind an obstacle, it is known that there is a counter-rotating eddy in the corner of the step. The standard k-ε model is generally considered to be incapable of representing the correct dimension of the corner eddy, which leads to the above-mentioned difference in mean velocity profiles. As summarized in Table 1, the size of the corner eddy provided by the second-moment closure is about one step height in both cases, while the k-ε model underestimates it by a factor of four.

Figure 4 shows that the turbulence intensity is appreciably underestimated in the upper half of the channel at most of the streamwise locations. On the other hand, the better results, shown in Figure 5, are calculated for the case of the higher channel by both turbulence models.

Pressure distributions

Figure 6 shows the distributions of wall-static pressure on the flat and serrated walls in the form of pressure coefficient C_P defined as $(P - P_0)/(1/2\rho U_m^2)$, with the reference pressure P_0 being measured on the flat side at $x/H_S = 0$. For both cases, the

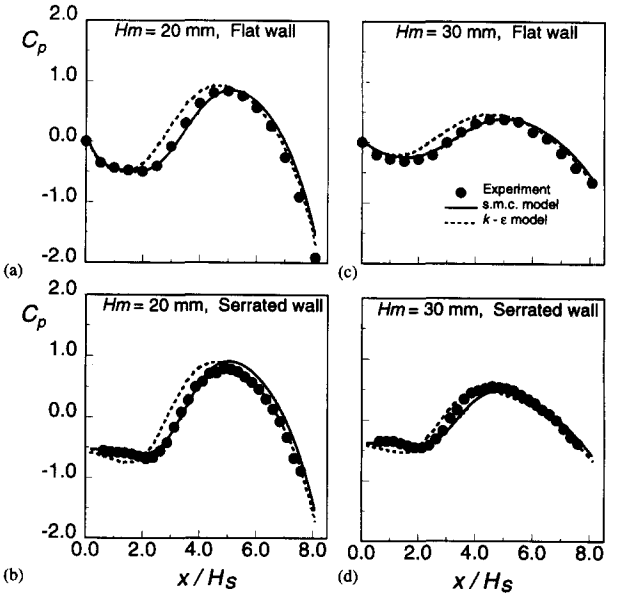

Figure 6 Wall static pressure distribution: (a) $H_m = 20$ mm, along the flat wall; (b) $H_m = 20$ mm, along the serrated wall; (c) $H_m = 30$ mm, along the flat wall; (d) $H_m = 30$ mm, along the serrated wall

general feature of the pressure distribution is characterized by the increase around the reattachment point due to the retardation of maximum velocity, followed by rapid decrease toward the next step because of the strong acceleration of mean flow due to the channel contraction. The distributions along the flat and serrated wall sides, Figures 6a and b for $H_m = 20$ mm and c and d for $H_m = 30$ mm, differ slightly from each other for $x/H_S \leqslant 4.0$; i.e., in the recirculation zone. The streamwise variation is less drastic for the higher channel, c and d, because of the smaller channel expansion ratio.

Provided that the mean flow direction is nearly parallel to the wall, the wall pressure distribution roughly corresponds to the variation of maximum mean velocity. Hence, the difference in pressure distribution due to the turbulence model is attributable to the different representation of streamwise flow development. In this sense, the fast pressure rise calculated using the k-ε model for $3 \leqslant H_S \leqslant 5$, Figure 6, reflects the rapid decrease in maximum mean velocity, see Figures 4a and 5a. This is considered to be a result of the excessive momentum transfer across the separated shear layer. On the other hand, the second-moment closure yields a better agreement with the experiment, which is also the case in backward-facing step flow (Obi et al. 1991). During the acceleration passage, there is no obvious difference between the results of the two turbulence models.

Since the momentum loss is an important factor in evaluating the performance of a heat exchanger, the pressure drop over a single step is compared with plane channel flow under the equivalent condition. The skin friction coefficient of plane channel flow can be calculated from the empirical relationship (e.g., Dean 1978), which yields the value of $C_f = 0.00697$ at the present Reynolds number. The nondimensional pressure drop

Table 1 Dimensions of the computed recirculation zone

	$H_m = 20$ mm		$H_m = 30$ mm	
	Primary	Secondary	Primary	Secondary
Second-moment closure	$3.91H_S$	$1.02H_S$	$3.75H_S$	$0.96H_S$
k-ε model	$3.84H_S$	$0.25H_S$	$3.60H_S$	$0.25H_S$

during the same distance as a single pitch of the serration (160 mm) is then calculated to be 0.056 and 0.037 for $H_m = 20$ mm and 30 mm, respectively. On the other hand, the nondimensional pressure drop in the serrated channel is 1.91 and 0.659 for $H_m = 20$ mm and 30 mm, obtained from the experiment (cf. Figures 6a and c). As a consequence, the serrated channel causes momentum loss that is higher than that in the plane channel by a factor of about 34 and 17 for the lower and higher channels, respectively. The results of calculations are well estimated for the pressure drop for $H_m = 30$ mm, but underestimated for $H_m = 20$ mm by about 10%. The k-ε model yields a slightly larger pressure loss. The resulting closer agreement with the data is thought to be coincidental; the reason the k-ε model provides more pressure drop is attributable to the excessive mixing of the separated shear layer. Unsatisfactory agreement between the computations and the experiment occurs, rather, during the acceleration passage, where the friction predominates the mixing loss. This points to the fact that a more realistic treatment of the boundary condition than the wall function is necessary for better calculation in this region.

Local Nusselt number distributions

Figure 7 shows local Nusselt number variation along both walls. Nusselt number Nu is defined as

$$\mathrm{Nu} = \frac{q_w H_m}{(T_w - T_b)\lambda} \tag{1}$$

where T_w and T_b are the wall temperature and the cross-sectional bulk temperature, respectively, and λ stands for the thermal conductivity of air. The peak value is achieved at about $x/H_s = 3.8$ on the serrated wall, while nearly uniform distributions are observed on the flat wall. It is found that the average Nusselt number increases with decreasing channel height along both walls, which is considered to be attributable to the stronger turbulence in the channel with lower height, as seen in Figures 4 and 5.

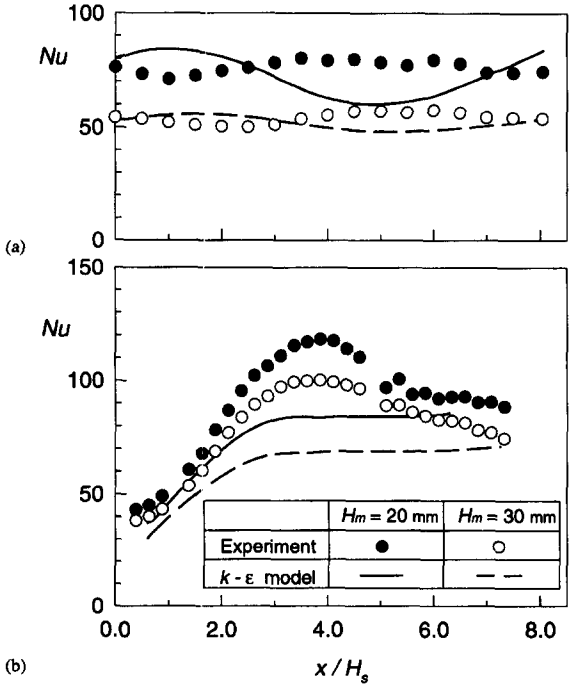

Figure 7 Nusselt number variation: (a) along the flat wall; (b) along the serrated wall

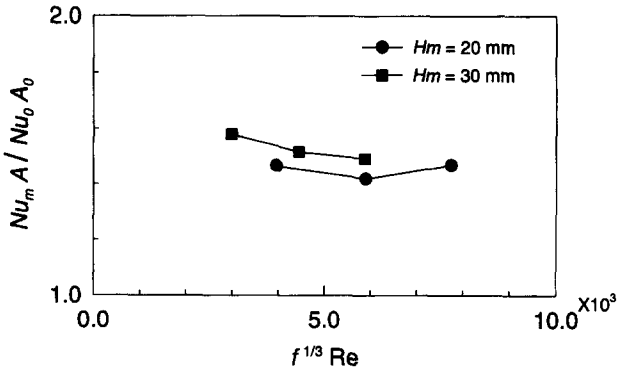

Figure 8 Measured heat transfer performance against pumping power

The heat transfer in plane channel flow at the same Reynolds number can be evaluated using the Dittus–Boelter correlation proposed for fully developed pipe flows; with the length scale converted from pipe diameter to hydraulic diameter of a plane channel, the average Nusselt number in a fully developed channel flow is calculated as 31.8. In the present experiment, the average Nusselt number over both sides of the wall are 84.0 and 67.3 for the lower and higher channels, respectively. Consequently, the factor of heat transfer promotion against plane channel flow is evaluated to be 2.64 and 2.11 for these two cases. According to the empirical relationship presented by Shishov et al. (1988), the Nusselt number at the reattachment point behind the backward-facing step is 48.9 at $\mathrm{Re} = 1.2 \times 10^4$. Compared to this value, it is seen that the present configuration provides higher heat transfer promotion than conventional backward-facing step flow. In addition to the heat transfer enhancement on the serrated wall, those along the flat wall are of comparable order for $H_m = 20$ mm; this is ascribed to the fact that the intense shear layer formed around the dividing streamline affected the wall-attached boundary layer along the flat wall.

Here, we discuss the heat transfer performance in terms of the required pumping power. Figure 8 shows the relative heat transfer enhancement against the 2-D channel flow as a function of the cube root of the pumping power $f^{1/3}\mathrm{Re}$, with f being the friction factor defined as $f = -(\mathrm{d}P/\mathrm{d}x)H_m/(1/2\rho U_m^2)$. Mean Nusselt number Nu_m is calculated by averaging over the entire heat transfer area where the increase in net area due to the serrated wall is taken into account. For both channel heights, it is indicated that the heat transfer rate is enhanced in the serrated channel flow by about 50%, although the pressure loss is large.

In the present study, the heat transfer calculations have been performed using the eddy viscosity model, with turbulent Prandtl number set equal to 0.9, combined with thermal wall function. Although this combination is most widely used in engineering applications, its shortcomings are well known (cf. Launder 1988). Hence, the comparison with the experiment is only qualitative. As shown in Figure 7, the computations underestimates the maximum Nusselt number on the serrated wall by over 30%, which is common in the wall function approach. On the flat-wall side, the agreement is achieved in terms of the average values over the single pitch. For both channel walls, the dependence on the channel height is represented. It should be noted that the marginal agreement thus obtained is not so discouraging if we take into account that the present flow field is susceptible to overwhelmingly strong turbulence.

Since the present configuration is aimed at the efficient use of the turbulent motion generated in the separated shear layer, it is of interest to investigate the relationship between the amount of turbulent kinetic energy and the heat transfer characteristics along

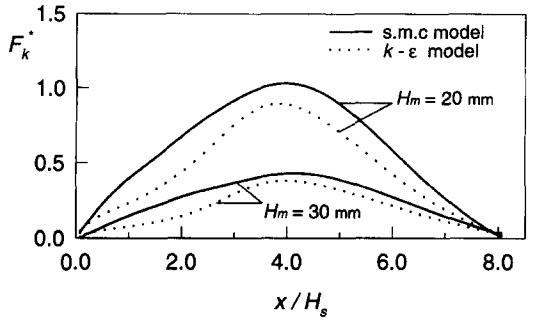

Figure 9 Streamwise variation of turbulent kinetic energy fluxes

the serrated wall. To this end, the turbulent energy flux F_k is evaluated from the computational results as a function of streamwise location:

$$F_k = \int_0^H Uk \, dy \tag{2}$$

where H is local channel height. Integrated over the channel cross section, the streamwise variation of F_k reflects the imbalance relative to the production and dissipation rates of k.

The plots in Figure 9 show the normalized difference $F_k^* = (F_k - F_{k0})/F_{k0}$, with F_{k0} being F_k at $x = 0$. It is understood that the turbulence energy generated along the separated shear layer up to the reattachment point diminishes during the acceleration passage down to the initial level, so that the overall energy equilibrium is realized within a serration pitch.

Since the separated shear layer is not in equilibrium, and its characteristics strongly influence the turbulent field around the flow reattachment region, it is expected that F_k and the heat transfer along the serrated wall are related. From Figures 7b and 9, it is seen that Nu is, indeed, closely related to the streamwise variation of F_k. The dependence on the channel height is also demonstrated. However, the difference due to turbulence models, which is discussed in terms of the mean velocity and turbulence intensity, (Figures 4 and 5) is not large.

Although the heat transfer enhancement in the serrated channel is a consequence of the turbulent fluid motion, it is inevitably associated with the considerable drawback due to pressure loss as the channel height is reduced. An extensive parameter study is necessary before the application of the present configuration to an actual heat exchanger.

Concluding remarks

A channel with a serrated wall has been proposed as a heat transfer promoter effective for both serrated and flat walls. The velocity measurements indicate that the flow characteristics partly resemble flows over a backward-facing step, although the turbulence level is higher because of successive flow separation and reattachment. The turbulence intensity increases with decreasing channel height; i.e., with increasing channel expansion ratio. Comparisons of measured heat transfer performance of the serrated channel with that for conventional channel flow demonstrate that the present configuration is promising as a new heat transfer element.

The calculated increase of turbulent kinetic energy in the separated shear layer is correlated with the measured heat transfer characteristics on the bottom wall on which the intensely turbulent fluid impinges, although the quantitative relationship remains unexplored. For realistic calculation of the heat transfer in this type of flow, the representation of turbulent shear layer development away from the wall is also of great importance. The basic version of the second-moment closures provides better agreement with the experiments as compared to the standard k-ε model. However, the difference is minor when compared in terms of an integral parameter, such as turbulent kinetic energy flux.

References

Armaly, B. F., Durst, F., Pereira, J. C. F. and Schönung, B. 1983. Experimental and theoretical investigation of backward-facing step flow. *J. Fluid Mech.*, **127**, 473

Driver, D. M. and Seegmiller, H. M. 1985. Features of a reattaching turbulent shear layer in divergent channel flow. *AIAA J.*, **23**, 163

Eaton, J. K. and Johnston, J. P. 1981. A review of research on subsonic turbulent flow reattachment, *AIAA J.*, **19**, 1093

Etheridge, D. W. and Kemp, P. H. 1978. Measurements of turbulent flow downstream of a rearward-facing step. *J. Fluid Mech.*, **86**, 545

Gibson, M. M. and Launder, B. E. 1978. Ground effects on pressure fluctuations in atmospheric boundary layer. *J. Fluid Mech.*, **86**, 491

Isomoto, K. and Honami, S. 1989. The effect of inlet turbulence intensity on the reattachment process over a backward-facing step. *J. Fluids Eng.*, **111**, 87

Kim, J., Kline, S. J. and Johnston, J. P. 1980. Investigation of a reattaching turbulent shear layer: Flow over a backward-facing step. *J. Fluids Eng.*, **102**, 302

Khosla, P. K. and Rubin, S. G. 1974. A diagonally dominant second-order accurate implicit scheme. *Computers Fluids*, **2**, 207

Launder, B. E. 1988. On the computation of convective heat transfer in complex turbulent flows. *J. Heat Transfer*, **110**, 1112

Launder, B. E. and Spalding, D. B. 1974. The numerical computation of turbulent flow. *Comp. Meth. Appl. Mech. Eng.*, **3**, 269

Obi, S. and Perić, M. 1991. A co-located finite-volume method for non-orthogonal grid with a second-moment turbulence closure. *Proc. 4th International Symposium CFD*, Davis, CA

Obi, S., Perić, M. and Scheuerer, G. 1991. Second-moment calculation procedure for turbulent flows with collocated variable arrangement. *AIAA J.*, **29**, 585

Patankar, S. V. and Spalding, D. B. 1972. A calculation procedure for heat, mass and momentum transfer in three-dimensional parabolic flows. *Int. J. Heat Mass Transfer*, **15**, 1787

Shishov, E. V., Roganov, P. S., Grabarnik, S. I. and Zabolotsky, V. P. 1988. Heat transfer in the recirculating region formed by a backward-facing step, *Int. J. Heat Mass Transfer*, **31**, 1557

Tropea, C. 1983. Die turbulente Stufenströmungen in Flachkanälen und offenen Gerinnen. Ph.D. dissertation, University of Karlsruhe, Karlsruhe, Germany